



Interstitial carbon-platinum electronic metal-support interaction structure boost synergistic removal of O₃ and CH₃SH via surface atomic oxygen

Dingren Ma^a, Jing Cao^a, Kairui Liu^c, Yexing Zhang^a, Qiwen Liang^a, Yajing Huang^a, Xinyi Guan^a, Lingling Hu^a, Chun He^{a,b}, Dehua Xia^{a,b,*}

^a School of Environmental Science and Engineering, Sun Yat-sen University, Guangzhou 510275, China

^b Guangdong Provincial Key Laboratory of Environmental Pollution Control and Remediation Technology, Guangzhou 510275, China

^c Advanced Membranes and Porous Materials Center, Physical Sciences and Engineering, King Abdullah University of Science and Technology, Thuwal 23955-6900, Saudi Arabia

ARTICLE INFO

Keywords:

Interstitial C

Dual-site catalytic structure

Electronic metal-support interaction

Surface atomic oxygen

ABSTRACT

Carbon atoms in the interstitial sites of metal nanoparticles have strong influence on heterogeneous catalysis via electronic metal-support interactions (EMSI). Here, the Pt catalysts with interstitial C-Pt EMSI structures were first developed and identified to boost the removal of ozone (O₃) and methyl mercaptan (CH₃SH). Experimental results showed that the intrinsic activity of the catalysts with low Pt loading (wt%, 0.95 %) was 186 times higher than that of commercial MnO₂. This excellent catalytic performance was attributed to dual-site catalytic structures to promote the adsorption/activation of O₃ at interstitial C and capture/oxidation of CH₃SH at Pt simultaneously. More importantly, the interstitial C sites retained surface atomic oxygen (*O) with excellent reactivity and lowered the energy barrier of C—S bond breakage, thus achieving efficient decomposition of CH₃SH into CO₂/SO₂. This work provides high-performance catalysts and new mechanistic insights for the synergistic control of O₃ and CH₃SH.

1. Introduction

In recent years, severe warm-season ozone (O₃) pollution is occurring with increasing frequency in both developing and developed countries due to the great global industrial development [1]. For example, the observed hourly maximum O₃ concentrations in China often exceed 150 ppb [2]. The World Health Organization has recommended that maximum O₃ concentrations in ambient air of more than 100 µg m⁻³ (~ 51 ppb) for 8 h pose threats to human health [3]. Ground-level O₃ is mainly generated by photochemical reactions between nitrogen dioxides and volatile organic compounds (VOCs) in the atmosphere under sunlight [4]. Notably, besides widely reported VOCs of aldehydes and benzene, sulfur-containing VOCs (S-VOCs) are also commonly found in the coal/natural gas industry and especially in the refuse landfill, which are not only involved in the formation of O₃ but are also one of the main sources of air odor pollution and sulfate aerosols, especially methyl mercaptan (CH₃SH) with a low olfactory threshold and ppb-ppm levels of emission concentrations [5–7]. The coexistence of O₃ and CH₃SH in the atmosphere further raises the risk of

potential respiratory and cardiovascular mortality. The simultaneous removal of O₃ and CH₃SH has thus become a global pursuit.

Catalytic O₃ decomposition for CH₃SH removal has been reported to be an effective and economic co-control technology owing to its advantages of high efficiency, enhanced mineralization, and mild operating conditions [6,8,9]. However, the practical catalytic performance is limited by the low dispersion and the insufficient catalytic activity of active sites [10,11]. Actually, the electronic metal-support interaction (EMSI) proposed by Campbell can improve these two factors of catalysts simultaneously [12,13]. As reported, the EMSI effect can disperse and stabilize active centers to expose more active sites, as well as induce electron transfer between the metal and support, modulate the electronic state and d-band center of the supported metal to optimize the intrinsic activity of each active site, thus often leading to excellent catalytic activity [14]. Therefore, it is promising to develop catalysts with strong EMSI.

Carbon materials are effective supports for constructing the EMSI effect due to their electrical conductivity and modulation of the electronic structure of active metals [13,15,16]. Interestingly, many

* Corresponding author at: School of Environmental Science and Engineering, Sun Yat-sen University, Guangzhou 510275, China.

E-mail address: xiadehua3@mail.sysu.edu.cn (D. Xia).

<https://doi.org/10.1016/j.apcatb.2023.122578>

Received 1 January 2023; Received in revised form 2 March 2023; Accepted 3 March 2023

Available online 5 March 2023

0926-3373/© 2023 Elsevier B.V. All rights reserved.

researchers have recently identified that C atoms can dissolve in metal nanoparticles and transfer between the surface and subsurface regions of metal grain boundaries, and work as a promoter rather than poison for catalytic reactions [17,18]. For instance, Wan et al. employed C atoms to occupy interstitial sites in the Au lattice, thus promoting electron transfer between C and Au and improving 3-nitrostyrene chemoselective hydrogenation performance [16]. Teschner and Rinaldi et al. found that interstitial C atoms could locally distort the geometrical/electronic structure of Pd and that EMSI structures based on covalent Pd—C bonds exhibited high reactivity to surface O and H adatoms to modulate catalytic alkyne hydrogenation reactions [19]. Motivated by these works, we contend that incorporating C atoms into the lattice interstitial sites of metals facilitates catalytic O_3 decomposition since the interstitial C atoms can gather delocalized electrons from metal atoms to promote the formation of electron-rich sites for surface O adsorption (like O_2/O_3) and work as electron shuttles to efficiently activate O_3 [20–22]. Very recently, since Pt itself is a high-performance catalyst owing to its unoccupied 5d-orbitals and strong adsorption/activation ability for reactants, our team developed an atomic Pt/graphene catalyst to accelerate catalytic ozonation for CH_3SH elimination [23]. In particular, the EMSI-structured Pt/graphene catalyst could promote the formation of Lewis acid sites for O_3 adsorption and maintain high activity via rapid circulation of Pt^{2+}/Pt^{4+} based on C—Pt covalent bonds [24,25]. However, the competing adsorption of CH_3SH and O_3 and the dispersion of the delocalized electrons of Pt sites made the catalytic activity cannot be further greatly enhanced. In contrast, interstitial C-Pt based catalysts are promising to overcome these limitations to optimize the EMSI effect for enhanced catalytic ozonation.

Generally, surface catalytic ozonation reactions that occur on active catalytic sites after adsorption like reactive oxygen species formation (ROSS, well reported $\cdot OH$, $\cdot O_2$, 1O_2 , etc.) directly determine mechanism-dependent activity and selectivity, but the role of surface oxygen species (surface atomic oxygen ($\cdot O$) and surface peroxide ($\cdot O_2$)) is always neglected [22]. Actually, $\cdot O$ and $\cdot O_2$ are key intermediates after O_3 adsorption/decomposition for other ROSS formation and has been proven to have the mineralization potential for organics (widely reported at average 2.43 V for $\cdot O$ and 1.35 V for $\cdot O_2$, respectively) [26–28]. However, the high reactivity of $\cdot O$ drives its rapid conversion. It is important to construct $\cdot O$ research platforms to reveal the conversion pathway of $\cdot O$ and tune the state of $\cdot O$, even to the extent that highly reactive $\cdot O$ is directly involved in reactions. Interestingly, interstitial C atoms have been proven to exhibit high reactivity towards surface O adatoms [29]. It is reasonable to propose that interstitial C atoms can be employed as platforms to investigate the electron shuttling between interstitial C atoms and $\cdot O/\cdot O_2$, as well as the effect of the reactivity of $\cdot O/\cdot O_2$ on catalytic ozonation for CH_3SH oxidation. Therefore, the generated ROSS and their role for catalytic ozonation need to be further identified over the interstitial C-Pt catalyst.

In this study, porous carbon nanospheres supported Pt catalysts with interstitial C-Pt EMSI structures (C-Pt/PCN) were first developed and identified to boost synergistic removal of O_3 and CH_3SH . X-ray photoelectron spectroscopy (XPS), electron energy loss spectroscopy (EELS), and synchrotron X-ray absorption spectroscopy (XAS) characterization were used to confirm the interstitial C-Pt EMSI structure. The roles of the interstitial C-Pt EMSI structure in gathering delocalized electrons, shuttling electrons to O_3 , triggering and retaining $\cdot O$, and lowering energy barriers were explained via in-situ Raman and in-situ diffuse reflectance infrared Fourier transform spectroscopy (in-situ DRIFTS) together with the density functional theory (DFT) calculations of the catalysts. This work highlights the remarkable potential of the interstitial C-Pt EMSI-based catalysts with low Pt loading for the synergistic removal of O_3 and CH_3SH and provides insights for the design of high-performance EMSI-based catalysts.

2. Experimental section

The details of characterization, synthesis of catalysts, experimental procedures, and theoretical calculations were shown in the [Supporting information](#).

2.1. Synthesis of catalysts

Porous carbon nanospheres (PCN) supported Pt catalysts with interstitial C-Pt EMSI structures (C-Pt/PCN) were synthesized by hydrothermal synthesis, polymerization for phenolic resins, and carbonization. By changing the amount of H_2PtCl_6 solution (4 mg mL^{-1}) while keeping the other processing parameters constant, PCN (0 mL of H_2PtCl_6), C-Pt/PCN1 (1.1875 mL of H_2PtCl_6), C-Pt/PCN2 (2.375 mL of H_2PtCl_6), C-Pt/PCN3 (4.75 mL of H_2PtCl_6), and C-Pt/PCN4 (9.5 mL of H_2PtCl_6) were obtained.

In contrast, reference carbon nanospheres (CN) supported Pt catalysts (Pt/CN) were prepared by an impregnation method. First, carbon nanospheres (CN) were synthesized by hydrothermal glucose solution. Then, Pt nanoparticles were loaded on CN by the impregnation-reduction method. The obtained black product was denoted Pt/CN.

2.2. O_3 decomposition measurement

O_3 decomposition tests were conducted with a continuous-flow fixed-bed reactor ([Fig. S1](#)) of the samples at room temperature (25°C) and the inlet gas flow rate of 1 L min^{-1} . A mixture of 20 mg of the samples and 180 mg of quartz sand (40–60 mesh) was loaded into the fixed-bed reactor and immobilized by quartz wool. O_3 in the inlet gas was generated by an O_3 generator (YDG, YE-TG-02PII), and its concentration (1 ppm) was controlled by the flow rate of air. The inlet (C_0) and outlet (C) concentrations of O_3 were continuously monitored via an O_3 sensor (2B Model, 106-M).

2.3. Synergistic removal tests of O_3 and CH_3SH

Synergistic removal tests of O_3 and CH_3SH were conducted with the continuous-flow fixed-bed reactor ([Fig. S1](#)) of the samples at room temperature (25°C) and the inlet gas flow rate of 100 mL min^{-1} . The humidity of inlet gas was controlled by a humidity generator. 20 mg of the samples were loaded into the fixed-bed reactor and immobilized by quartz wool. 500 ppm of O_3 was generated by an O_3 generator (YDG, YE-TG-02PII), and the flow rate of O_3 in the system was controlled at 10 mL min^{-1} . The inlet concentration of CH_3SH was maintained at about 50 ppm by diluting 1000 ppm of CH_3SH (balanced using N_2) with clean air. The inlet (C_0) and outlet (C) concentrations of CH_3SH were continuously monitored via a CH_3SH sensor (Detcon, DM-400IS). The outlet gas was collected with gas bags and the gas compositions were identified by Proton Transfer Reaction Time-of-Flight Mass Spectrometer (PTR-TOF-MS, PTR-TOF 1000, Ionicon Analytik GmbH, Austria). Residual O_3 concentration in the outlet gas was detected using the PTR-TOF-MS due to the flow limitation of the O_3 sensor.

3. Results and discussion

3.1. Formation of interstitial C-Pt EMSI structures

The morphology of C-Pt/PCN3 and Pt/CN with similar Pt loading (0.95–1.41 wt% in [Table S1](#)) was shown in [Fig. 1](#). Pt nanoparticles in C-Pt/PCN3 were embedded in porous carbon nanospheres ([Fig. 1a–b](#) and [S2a](#)), while Pt nanoparticles in Pt/CN were deposited on the surface of carbon nanospheres ([Fig. 1d–e](#) and [S2b](#)). It has been reported that the lattice contraction occurs in the Pt nanoparticles and is proportionally reciprocal to the size of Pt nanoparticles [16]. However, the Pt (111) spacing increased from 0.217 nm for Pt/CN (the size of Pt nanoparticles = 3.07 nm, [Fig. 1f](#) and [S3b](#)) to 0.224 nm for C-Pt/PCN3 (the size of Pt

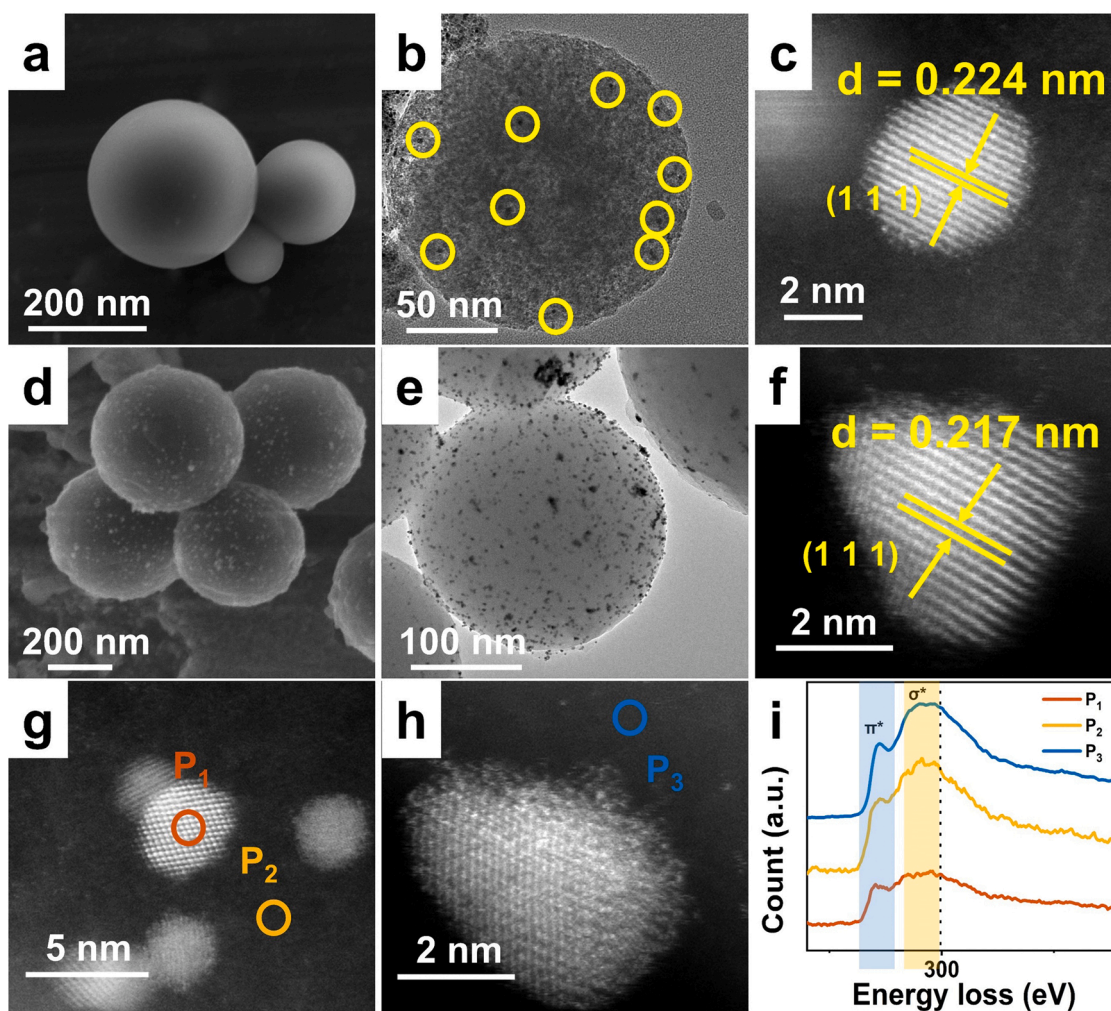


Fig. 1. Scanning transmission electron microscopy (STEM), transmission electron microscopy (TEM), and aberration-corrected high-angle annular dark-field scanning transmission electron microscopy (AC HAADF-STEM) images for C-Pt/PCN3 (a–c, g) and Pt/CN (d–f, h), respectively; (i) Electron energy-loss (EEL) C core-loss spectra. Numbering (Position 1–3, P₁–P₃) indicates where on the samples the EEL data was collected.

nanoparticles = 2.16 nm, Fig. 1c and S3a), which might be attributed to the fact that C atoms were anchored in the Pt (111) lattice interstice causing the swell of the Pt (111) lattice. During the synthesis of C-Pt/PCN3, phenolic resins and triblock copolymers decomposed at high temperatures (700 °C) into small methane (CH₄) molecules, followed by the decomposition of CH₄ leading to the dissolution of C atoms in Pt nanoparticles [30–32]. As identified, with a height of 27–41 kJ mol^{−1}, the relatively low sinking energy barrier of C atoms in Pt nanoparticles enhances C atoms transfer between the surface and subsurface regions at Pt grain boundaries [32]. The continuous exchange of C atoms between the surface and subsurface regions of Pt nanoparticles established a dynamic equilibrium that led to a relatively uniform lattice expansion of Pt nanoparticles in C-Pt/PCN3. To verify the dissolution of C atoms into the lattice interstitial sites of Pt nanoparticles, Fig. 1g–i and S4 displayed the EELS from various positions of aberration-corrected high-angle annular dark-field scanning transmission electron microscopy (AC HAADF-STEM) images and provided qualitative evidence of the electronic state of the C element in the Pt nanoparticles and the C matrixes [33]. For the carbon matrixes of C-Pt/PCN3 and Pt/CN (Position 2 of Fig. 1g and Position 3 of Fig. 1h, P₂ and P₃), the electron energy loss near the edge structure of the C-K edge consisted of two energy loss peaks ($1s \rightarrow \pi^*$ transition peak at 286 eV and $1s \rightarrow \sigma^*$ transition peak at 295 eV), similar to that of the amorphous carbon [34]. In contrast, there was no carbon peaks present in the Pt nanoparticle of Pt/CN, as shown in Fig. S4. For the Pt nanoparticle of C-Pt/PCN3 (Position 1 of Fig. 1g, P₁),

two energy loss peaks similar to those of P₂ and P₃ were observed, indicating the presence of C species on the surface of the Pt nanoparticle. More importantly, the intensity of the σ^* edge of P₁ was significantly reduced, from which we could deduce that C atoms were dissolved into the Pt lattice and were strongly bound to Pt atoms [34]. Moreover, P₁ exhibited a peak at 300 eV (dotted line), revealing a unique coordination structure of C atoms that differed from the sp^2 structure of C in the carbon matrixes [35].

The lattice expansion and strong binding induced by interstitial C atoms were further reflected in X-ray diffraction (XRD) and XPS. The phase information of the samples was shown in Fig. 2a. The two broad diffraction peaks at around 22° (002, graphite) and 44° (101, graphite) were attributed to the disordered and defective C structures [36]. The diffraction peak at around 39° was indexed to the Pt (111) plane and increased in intensity with increasing Pt loading [37]. The intensity of the Pt (111) peak of Pt/CN was significantly enhanced due to the exposure of Pt nanoparticles. As expected, the Pt (111) peak of C-Pt/PCN3 was shifted to a lower angle compared to Pt/CN, revealing the lattice expansion of Pt nanoparticles in C-Pt/PCN3 [38]. The surface chemical states of the samples were revealed by XPS (Fig. 2b and Table S2). The binding energy of Pt⁰ of C-Pt/PCN3 (71.8 eV) was higher than that of Pt/CN (71.5 eV), mainly attributed to the strong binding between the C and Pt atoms and more specifically to the electron transfer from the Pt atoms to the interstitial C atoms [16].

To elucidate the electronic structure and the coordination

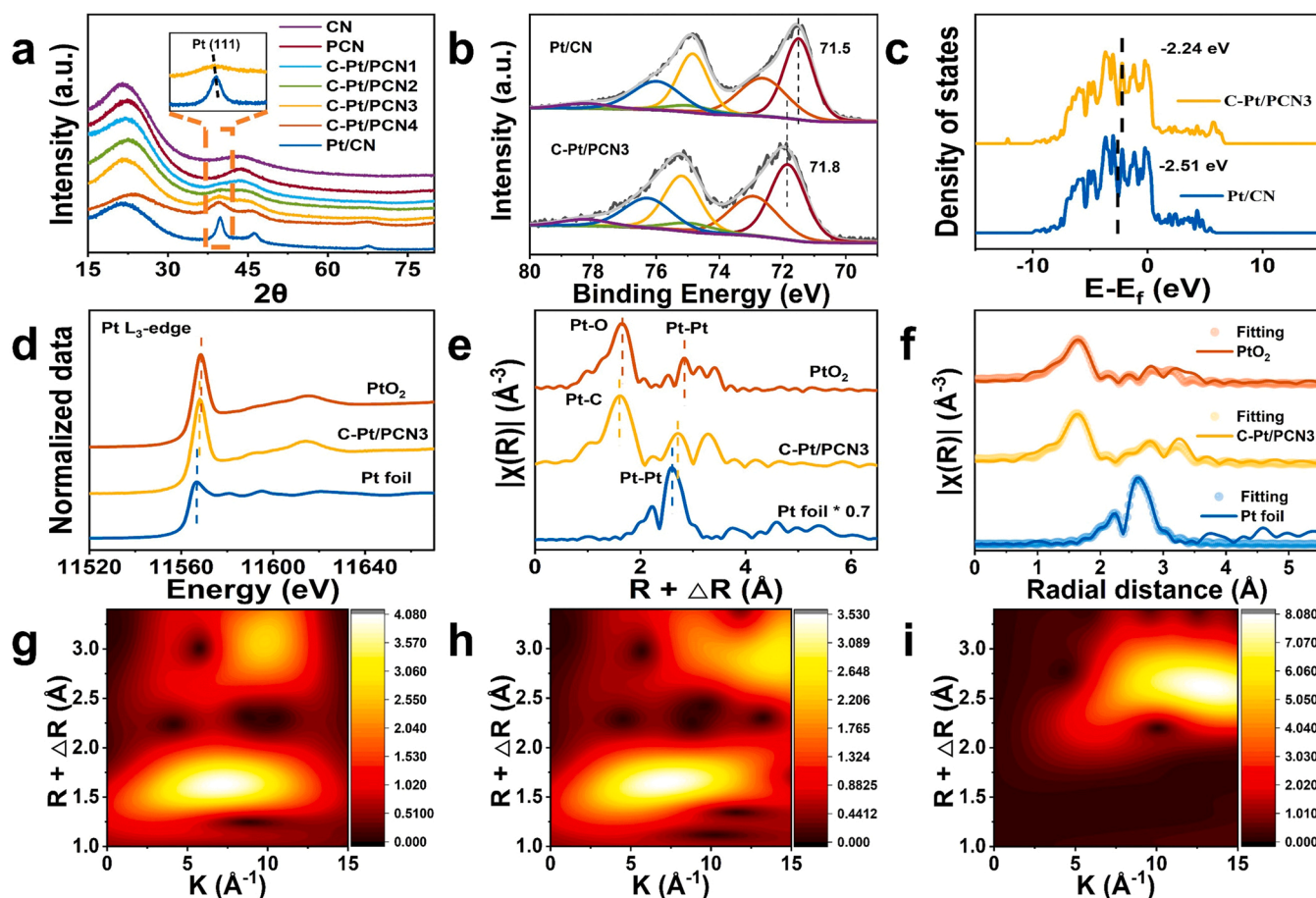


Fig. 2. (a) X-ray diffraction (XRD) patterns of the samples; (b) X-ray photoelectron spectroscopy (XPS) of Pt 4f of C-Pt/PCN3 and Pt/CN; (c) The *d*-band center of C-Pt/PCN3 and Pt/CN; (d) Pt L₃-edge X-ray absorption near-edge structure (XANES) spectra for Pt foil, PtO₂ and C-Pt/PCN3; (e) The *k*₂-weighted $\chi(k)$ -function of the extended X-ray absorption fine structure (EXAFS) spectra for Pt foil, PtO₂ and C-Pt/PCN3; (f) Corresponding EXAFS fitting curves of Pt foil, PtO₂ and C-Pt/PCN3 at *R* space; Wavelet transform of Pt L₃-edge EXAFS data for C-Pt/PCN3 (g), PtO₂ (h) and Pt foil (i).

environment of C-Pt/PCN3, XAS was further employed. The X-ray absorption near-edge structure (XANES) spectra of the Pt L₃-edge (Fig. 2d) revealed the average oxidation states of Pt. The Pt average oxidation state in C-Pt/PCN3 was between that in Pt foil and PtO₂ due to the electron transfer from the Pt atoms to the interstitial C atoms and the partial oxidation of Pt nanoparticles [39]. The Fourier-transformed (FT) *k*²-weighted extended X-ray absorption fine structure (EXAFS) profiles were used to probe the local environment of Pt (Fig. 2e). For C-Pt/PCN3, the main peak at ≈ 1.6 Å corresponded to the Pt-C coordination, which was shorter than the Pt-O (≈ 1.7 Å) coordination of PtO₂. More importantly, C-Pt/PCN3 displayed the Pt-Pt coordination at 2.7 Å, which was higher than that of Pt foil (2.6 Å) and lower than that of PtO₂ (2.8 Å), indicating that the C atoms occupied the interstitial sites to expand the Pt lattice. The wavelet transforms (WT) of Pt L₃-edge EXAFS oscillations in Fig. 2g–i and the best-fit results of the EXAFS data in Fig. 2f and Table S3 further confirmed this conclusion. Combined with the aforementioned analysis, it was concluded that the interstitial C-Pt EMSI structure was formed in C-Pt/PCN3.

DFT calculations were further performed to provide theoretical support for the interstitial C-Pt EMSI structure [16,32]. The models of C-Pt/PCN3 and Pt/CN were shown in Fig. S6. The incorporation of the interstitial C atom expanded the length of the neighboring Pt–Pt bonds from 2.8 Å to 3.1 Å (theoretical result for the case of the fixed interstitial C atom). The deformation charge density and the Bader charge were used to visualize the direction and the specific number of transferred electrons, respectively. As shown in Fig. S7, the interstitial C atom gathered the delocalized electrons of the Pt atoms. Specifically, in the

interstitial C-Pt EMSI structure, the interstitial C atom gained 0.22 e, whereas the three surrounding Pt atoms each lost about 0.09 e, leading to a high electron density on the interstitial C atom. The electronic structures and orbital interactions were further illustrated by the projected density of states (PDOS). The wide and sharp Pt 5*d* band was involved in electron transfer and bonding reactions (Fig. S8) [40]. Notably, the C 2*p* band overlapped the Pt 5*d* band, indicating that the Pt 5*d* orbital covalently interacted with the C 2*p* orbital to form the C–Pt bonds via σ bonding [40]. Thus, the interstitial C-Pt EMSI structures were formed in C-Pt/PCN3 and promoted the electron transfer from Pt to C, resulting in a significant optimization of the electronic configuration of C-Pt/PCN3.

The optimization of the electronic configuration of C-Pt/PCN3 could be confirmed by the *d*-band center theory. The *d*-band center is a widely accepted descriptor in electronic structures to explain the activity trend of catalysts [41,42]. A higher *d*-band center results in a lower electron filling degree and stronger adsorption of reactants/intermediates, generally resulting in a higher catalytic activity [43]. Fortunately, the calculated *d*-band center of C-Pt/PCN3 (-2.24 eV) was higher than that of Pt/CN (-2.51 eV) (Fig. 2c), from which it was reasonable to deduce that C-Pt/PCN3 with the interstitial C-Pt EMSI structure could achieve better catalytic performance than Pt/CN.

3.2. Catalytic performance

O₃ dynamic decomposition tests over the samples were first performed. As shown in Fig. 3a, the O₃ decomposition efficiencies of all the

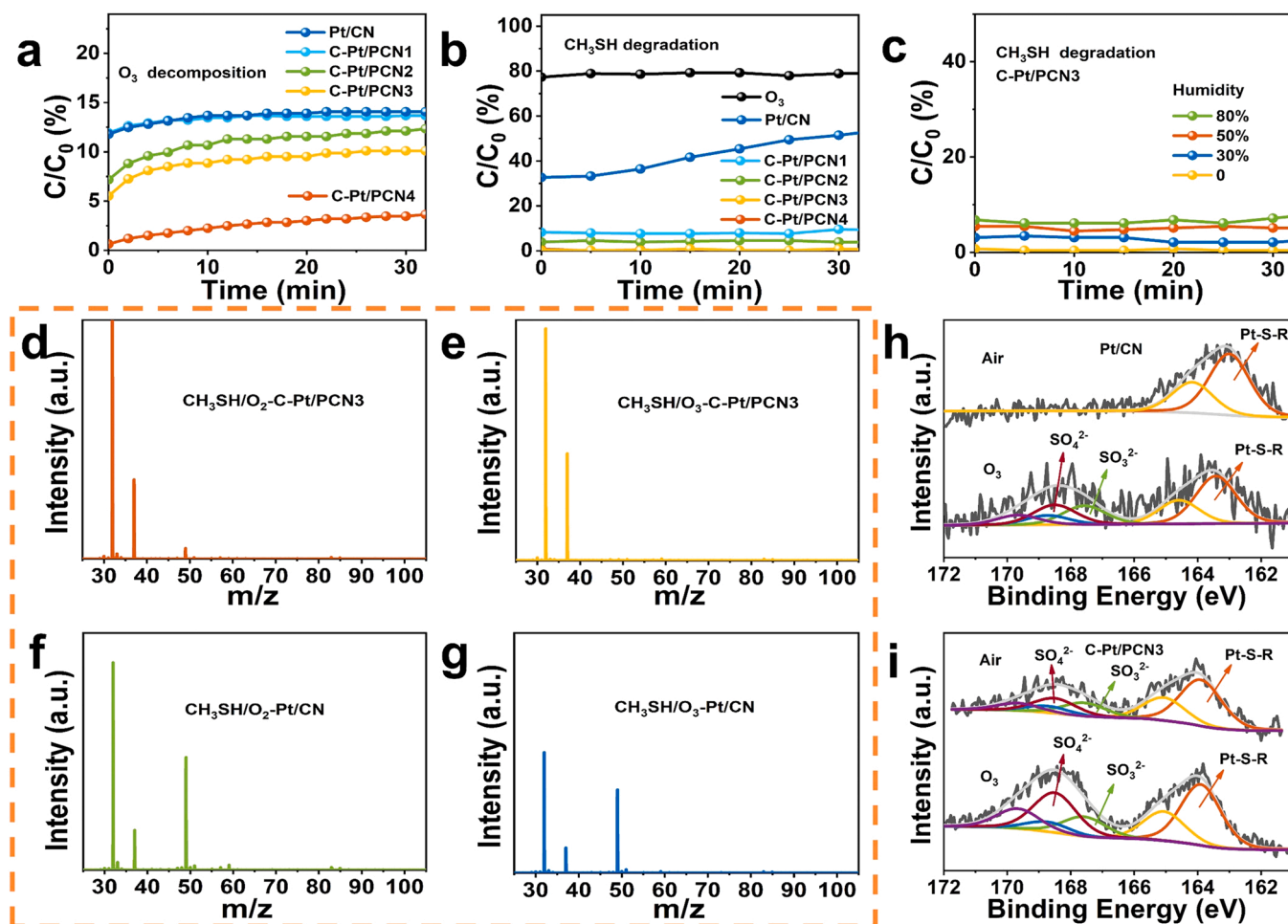


Fig. 3. (a) O_3 dynamic decomposition tests over the as-prepared catalysts; (b) CH_3SH dynamic catalytic ozonation tests over the as-prepared catalysts (the degradation curves of C-Pt/PCN3 and C-Pt/PCN4 overlapped); (c) CH_3SH dynamic catalytic ozonation tests over C-Pt/PCN3 under different humidity; The concentrations of CH_3SH , O_3 , and typical intermediates in the outlet gases of C-Pt/PCN3 (d, e) and Pt/CN (f, g) after the reactions for 30 min determined by proton transfer reaction time-of-flight mass spectrometry (PTR-TOF-MS); XPS spectra of S 2p of C-Pt/PCN3 (h) and Pt/CN (i).

C-Pt/PCN catalysts were higher than 86 %, with the highest O_3 decomposition efficiency of 96 % for C-Pt/PCN4. Notably, although the Pt loading of Pt/CN was theoretically 5.6 times higher than that of C-Pt/PCN1, the O_3 decomposition efficiency of Pt/CN was similar to that of C-Pt/PCN1. This result indicated that the interstitial C-Pt EMSI structure provided excellent O_3 decomposition activity. Interestingly, the samples were gradually deactivated due to the coverage of O_3 decomposition products on the surface of the samples, which will be discussed in Section 3.3.

CH_3SH dynamic adsorption and catalytic ozonation tests over the samples were performed. As shown in Fig. S9, the adsorption performance of PCN (38 %) was similar to that of CN (33 %) due to the similar specific surface area (Table S1, 520.60 and 536.75 $m^2 g^{-1}$), indicating that the different C matrixes had little effect on the performance. The loading of Pt nanoparticles greatly improved the adsorption performance of C-Pt/PCN3 and Pt/CN to 85 % and 65 %, respectively, which was mainly due to the chem-adsorption and even the partial oxidation via activated $*O_2$ on the surface of the samples [23]. The removal performance of C-Pt/PCN3 and Pt/CN decreased to 72 % and 25 % after 30 min, respectively, attributed to the rapid consumption of $*O_2$ and saturation of adsorption. These hypotheses will be further illuminated in Section 3.4.1. Then the O_3 was purged to trigger the ozonation process (Fig. 3b), and the catalytic ozonation performance of Pt/CN, C-Pt/PCN1, C-Pt/PCN2, C-Pt/PCN3, and C-Pt/PCN4 for CH_3SH degradation reached 67 %, 92 %, 96 %, 100 %, and 100 %, respectively, indicating that the

reactive oxygen species generated by catalytic ozonation were greatly involved in the oxidation reaction of CH_3SH . In contrast, only 21 % of CH_3SH removal was achieved by sole O_3 . Especially, the C-Pt/PCN catalysts maintained the high CH_3SH removal efficiencies for more than 30 min, while Pt/CN was greatly deactivated after 10 min. The results were further confirmed by the long-time catalytic tests. After 90 min of reaction, the CH_3SH degradation efficiency of C-Pt/PCN3 was maintained at 99 %, while that of Pt/CN decreased to 30 % (Fig. S12a). Notably, the CH_3SH degradation efficiency of C-Pt/PCN3 was maintained at 46 % after 3000 min of reaction (Fig. S12b). As shown in Fig. S12c–d, the specific and mass activities of C-Pt/PCN3 reached 2029 $ppm m^{-2}$ and 261 $ppm mg^{-1}$, respectively, which were significantly higher than those of Pt/CN (616 $ppm m^{-2}$ and 56 $ppm mg^{-1}$). Moreover, the mass activity of the C-Pt/PCN3 catalyst is 186 times higher than that of commercial MnO_2 (1.4 $ppm mg^{-1}$, Fig. S13 and Table S4) and even surpasses that of the single-atom Pt catalyst (0.5 CE-Pt-G, 111 $ppm mg^{-1}$) [23]. Moreover, turnover frequencies (TOFs) of CH_3SH removal over C-Pt/PCN3 and Pt/CN were further calculated. As shown in Table S5, the C-Pt/PCN3 catalyst achieved a TOF of 26.45 h^{-1} , much higher than that of the Pt/CN catalyst (TOF = 5.01 h^{-1}). Notably, most of the reported catalysts have lower TOF values than C-Pt/PCN3 [9,23]. Therefore, C-Pt/PCN3 with the interstitial C-Pt EMSI structures exhibited significantly enhanced performance.

The proton transfer reaction time-of-flight mass spectrometry (PTR-

TOF-MS) and XPS were used to further reveal the catalytic performance and distribution of catalytic products. For the adsorption process (Figs. 3d and 3f), the patterns exhibited that only one characteristic peak attributed to CH_3SH (49) (except for H_2O and O_2 (37 and 32)) was detected and the CH_3SH signal of C-Pt/PCN3 was much lower than that of Pt/CN. Correspondingly, the high contents of S species (Table S6) were detected on the surface of C-Pt/PCN3 (1 %) and Pt/CN (0.5 %). Interestingly, in the S 2p spectra (Fig. 3h–i), C-Pt/PCN3 showed three peaks at 163.9, 167.6, and 168.5 eV assigned to Pt-S-R, SO_3^{2-} , and SO_4^{2-} , respectively, while Pt/CN showed only one peak at 163.0 eV attributed to Pt-S-R, indicating the different degradation behavior of CH_3SH on the surface of the samples in the air. Combined with the results of Fig. S9, it could be reasonably inferred that Pt nanoparticles possessed excellent chem-adsorption for VOCs and the interstitial C-Pt EMSI structures triggered more active $\cdot\text{O}_2$ [9,44]. For the catalytic ozonation process (Figs. 3e and 3g), the CH_3SH signal of C-Pt/PCN3 and Pt/CN greatly decreased, indicating that CH_3SH was further removed. More importantly, O_3 (48), CH_3SH , and intermediates were not detected in the outlet gas of C-Pt/PCN3, indicating the excellent catalytic ability of C-Pt/PCN3 was involved. Table S6 showed that the content of SO_4^{2-} increased as the intermediates were further oxidized after O_3 purging. The higher SO_4^{2-} content on C-Pt/PCN3 (34 %) than that on Pt/CN (24 %) revealed that CH_3SH was more thoroughly mineralized on the surface of C-Pt/PCN3. In addition, more sulfur-containing species were deposited on the surface of C-Pt/PCN3 (1.2 %) than that of Pt/CN (0.6 %), further indicating that the catalytic activity and S species tolerance of C-Pt/PCN3 were better than Pt/CN. The degradation products and pathways of CH_3SH on the surface of the catalysts will be

discussed in Section 3.4.

Exposing metal-center active sites to reaction gases for elimination is an important factor, but these sites are easily occupied by other species in the air, particularly H_2O molecules, and are thus deactivated at high humidity [4]. To investigate the general applicability of the C-Pt/PCN catalysts, the influence of humidity on the catalytic performance of C-Pt/PCN3 was performed. As shown in Fig. 3c, the catalytic performance of C-Pt/PCN3 decreased with increasing humidity due to the competitive adsorption of H_2O molecules [23]. Interestingly, the catalytic performance of C-Pt/PCN3 still reached more than 90% under all humidity settings (from 0 % to 80 %), showing that C-Pt/PCN3 was suitable for most of the Earth environments. The discussion about the effect of humidity will be further mentioned in Section 3.4.2.

3.3. Mechanistic studies for O_3 conversion

Surface catalytic ozonation reactions that occur on active catalytic sites after adsorption directly determine mechanism-dependent activity and selectivity. Therefore, it is important to clarify the O_3 conversion pathway on the surface of the catalysts [23]. In-situ Raman was used to monitor the activation of O_3 on the active centers. As shown in Fig. 4a–b, C-Pt/PCN3 and Pt/CN had peaks (899 and 880 cm^{-1}) in the air attributed to $\cdot\text{O}_2$ with a redox potential of 1.35 V, indicating that C-Pt/PCN3 and Pt/CN could activate O_2 to degrade CH_3SH . Notably, the difference in $\cdot\text{O}_2$ peak positions might reveal the difference in the redox capacity and activation sites of $\cdot\text{O}_2$ over C-Pt/PCN3 and Pt/CN, which will be discussed in Section 3.4.1 [5]. For O_3 activation, a peak at 963 cm^{-1} attributed to $\cdot\text{O}$ emerged when C-Pt/PCN3 connected with O_3 [4,28,

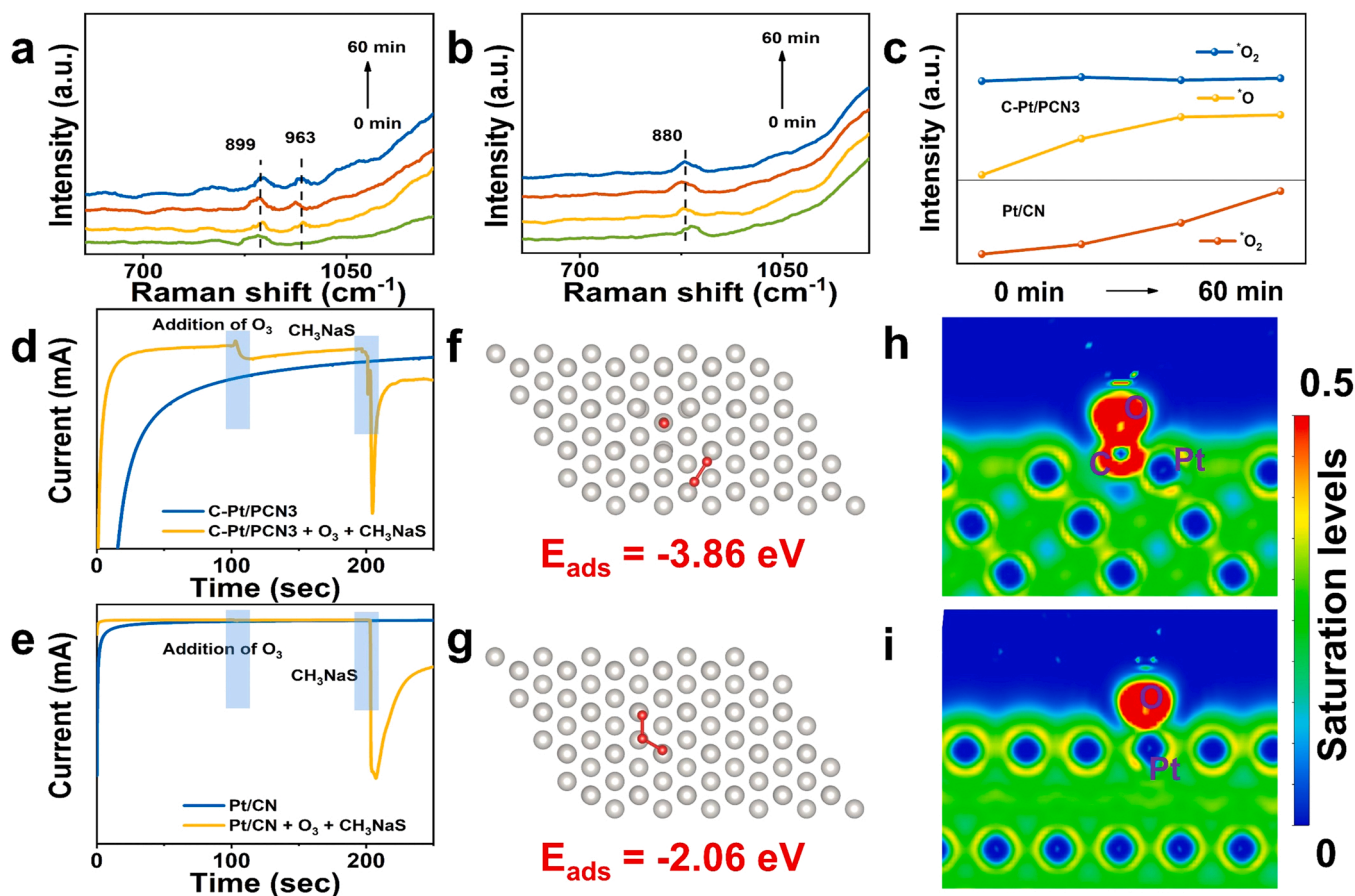


Fig. 4. In-situ Raman spectra of C-Pt/PCN3 (a) and Pt/CN (b) in the presence of O_3 ; (c) Trends in the intensity of the $\cdot\text{O}_2$ and $\cdot\text{O}$ peaks of C-Pt/PCN3 and Pt/CN with time; The chronoamperometry curves on C-Pt/PCN3 (d) and Pt/CN (e); The optimized adsorption of O_3 molecule on C-Pt/PCN3 (f) and Pt/CN (g) coordination structures; Electron localization function of C-Pt/PCN3 (h) and Pt/CN (i) with $\cdot\text{O}$. All lengths are given in Å. The silver, red and brown balls denote Pt, O and C atoms, respectively. The blue and yellow isosurfaces represent charge accumulation and depletion in the space, respectively.

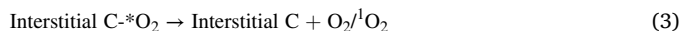
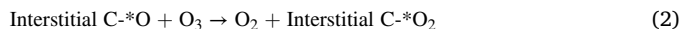
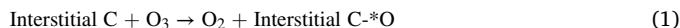
45]. However, no characteristic peak assigned to *O was observed on the surface of Pt/CN in Fig. 4b, which was due to the rapid conversion of *O . It has been reported that *O rapidly reacts with O_3 to form *O_2 [26]. And *O_2 is the most abundant reaction intermediate in the decomposition reaction of O_3 due to the slow desorption of *O_2 on the surface of catalysts [26]. This conclusion was consistent with our findings, as the intensity of the *O_2 peak on the surface of Pt/CN increased rapidly with time in Fig. 4c. Interestingly, the stable *O_2 peak and the rapidly enhancing *O peak were observed on the surface of C-Pt/PCN3, indicating that the interstitial C-Pt EMSI structures helped to retain *O and inhibited the conversion of *O to *O_2 [28]. It was worth mentioning that the abundance of *O and *O_2 on the surface of Pt/CN and C-Pt/PCN3 was the main reason for the low efficiency of O_3 decomposition and rapid deactivation. In addition, the singlet oxygen (1O_2) intensity of C-Pt/PCN3 was much lower than that of Pt/CN (only 1O_2 was detected in this work, Fig. S14), confirming that *O was retained by the interstitial C-Pt EMSI structures. Combined with the catalytic performance results, *O and *O_2 were involved in the oxidation of CH_3SH . More importantly, *O played a critical role in CH_3SH degradation.

The critical role of *O in CH_3SH degradation was further investigated by the electrochemical analyses [46]. As shown in Fig. S15, adding the CH_3NaS solution or saturated O_3 solution to the system without samples did not cause a change in the current. When the saturated O_3 solution was introduced in the C-Pt/PCN3 system in Fig. 4d, the current increased instantaneously and then decreased, indicating that O_3 gained electrons from C-Pt/PCN3 and then generated interstitial C- *O complexes. Subsequently, the added CH_3NaS donated electrons and reacted with the complexes, leading to a rapid drop in the current. In contrast, the current fluctuation of the Pt/CN system was weak when the saturated O_3 solution was added (Fig. 4e), which was attributed to the weak activation of O_3 and the fast conversion of *O . This conclusion was further confirmed by the weak current variation induced by the subsequent addition of the CH_3NaS solution. Therefore, *O played a greater role in the oxidation of CH_3SH . Moreover, CH_3SH could react with *O and *O_2 to achieve the synergistic degradation of O_3 and CH_3SH .

DFT calculations were used to further illustrate the reactivity of $^*O/^*O_2$. As shown in Fig. 4f-g, the adsorption energy of O_3 of C-Pt/PCN3 (-3.86 eV) was lower than that of Pt/CN (-2.06 eV) since the interstitial C atom with high electron density preferentially adsorbed the electrophilic O_3 molecules. Moreover, the O—O bond of C-Pt/PCN3 (3.33 Å) was much longer than that of Pt/CN (1.41 Å), indicating that O_3 adsorbed on the surface of C-Pt/PCN3 was easily decomposed to generate *O and O_2 [26]. These results confirmed the excellent O_3 decomposition efficiencies of the C-Pt/PCN catalysts in Fig. 3a. The interfacial electron transfer between the samples and *O was further calculated. *O anchored on the interstitial C atom obtained 0.92 e from C-Pt/PCN3 (Fig. S16a), whereas *O anchored on the Pt atom only obtained 0.54 e from Pt/CN (Fig. S16b), indicating that the interstitial C atom worked as an electron shuttle to generate more reactive *O . Notably, Pt atoms on the surface and subsurface of Pt/CN were involved in the electron donation to *O , while *O on the surface of C-Pt/PCN3 had little effect on the electronic structure of Pt nanoparticles, indicating that the interstitial C-Pt EMSI structure improved the utilization efficiency of delocalized electrons of Pt atoms and shortened the electron transport path between O_3 and the surface of C-Pt/PCN3. Moreover, in contrast to the electron depletion between the Pt atom and *O on Pt/CN, there was electron accumulation between the interstitial C atom and *O on C-Pt/PCN3, confirming that *O was retained by the interstitial C. This conclusion was further confirmed by the electron localization function in Fig. 4h-i. The strong binding between the interstitial C atom and *O inhibited the rapid conversion of *O to lower oxidative $^*O_2/^1O_2$. The reactivity of *O_2 was also calculated, and the results were shown in Fig. S17. Similarly, the *O_2 molecule adsorbed on the interstitial C atom exhibited the adsorption energy of -1.89 eV and the O—O bond length of 1.47 Å, indicating that C-Pt/PCN3 triggered more reactive *O_2 than Pt/CN (-1.82 eV, 1.37 Å). These results were consistent with the

experimental tests.

In short, the interstitial C-Pt EMSI structure promoted the electron transfer from the Pt atoms to the interstitial C atom to gather the delocalized electrons of Pt atoms, shortened the electron transport path to O_3 , decomposed O_3 to generate *O , and retained *O with excellent reactivity. The activation pathway of O_3 on the surface of C-Pt/PCN3 could be presented by the following equations (Eqs. (1)–(3)).



3.4. Mechanistic studies for CH_3SH elimination

The interstitial C atoms worked as electron shuttles to activate O_3 to generate *O , which efficiently degraded CH_3SH . To analyze the rapid degradation pathway of CH_3SH on the interstitial C-Pt EMSI structures, in-situ DRIFTS was used to monitor the intermediates in the reaction processes. The intermediates corresponding to the characteristic peaks were listed in Table S7.

3.4.1. Adsorption period

Fig. 5a and c showed the adsorption behavior of CH_3SH on C-Pt/PCN3 and Pt/CN, respectively. The appearance of the S—O bonds (896 , 862 , and 808 cm^{-1}) indicated that CH_3SH reacted with surface oxygen-containing functional groups such as activated *O_2 [47]. As mentioned above, the *O_2 reactivity of C-Pt/PCN3 was expected to be considerably different from that of Pt/CN. The retention of the S—H bonds (2573 cm^{-1}) and the absence of SO_4^{2-} (1263 cm^{-1}) and CH_2O (1518 cm^{-1}) on the surface of Pt/CN confirmed the hypothesis [5]. Moreover, it could be reasonably inferred from the above results that the breakage of the C—S bonds might be the rate-limiting step for CH_3SH degradation.

The CH_3SH adsorption energies of C-Pt/PCN3 and Pt/CN were calculated. As shown in Fig. 5e and S18, the CH_3SH adsorption energy of C-Pt/PCN3 (-1.89 eV) was greater than that of Pt/CN (-1.93 eV), indicating that the excellent adsorption performance of C-Pt/PCN3 in Fig. S9 was due to more active *O_2 triggered by the interstitial C-Pt EMSI structures. Notably, the adsorption energies of CH_3SH at different adsorption sites of C-Pt/PCN3 were different. As shown in Fig. S19, the Pt site farthest from the interstitial C atom had the strongest adsorption of CH_3SH . Therefore, O_2/O_3 was preferentially adsorbed on the interstitial C site, while CH_3SH was adsorbed on the Pt site, forming a unique dual-site catalytic structure and promoting the synergistic removal of CH_3SH and O_3 .

3.4.2. Catalytic ozonation period

After the introduction of O_3 , the removal of CH_3SSCH_3 (968 cm^{-1}) and the accumulation of SO_4^{2-} (1268 cm^{-1}) in Fig. 5b showed that the generated *O further oxidized the intermediates on the surface of C-Pt/PCN3 [9]. Actually, the deposition of SO_4^{2-} on the surface of catalysts was the major cause of deactivation [6]. In comparison to C—Pt/PCN3, the S—H bonds (2573 cm^{-1}) disappeared and CH_4O_3S (1200 and 1056 cm^{-1}) gradually accumulated on the surface of Pt/CN with the introduction of O_3 (Fig. 5d) [6]. Notably, products such as $HCOOH$ (1741 cm^{-1}) and SO_4^{2-} (1268 cm^{-1}) were not detected, indicating that the rate-limiting step for CH_3SH degradation was the breakage of the C—S bonds [48]. The large number of intermediates deposited on the surface of Pt/CN resulted in poor durability of Pt/CN (Fig. 3b).

As identified, the breakage of the C—S bonds was the rate-limiting step for CH_3SH degradation, and the Gibbs free energy of the breakage of the C—S bonds was calculated. As shown in Fig. 5f and S20, the breakage of the C—S bonds on the surface of Pt/CN could not

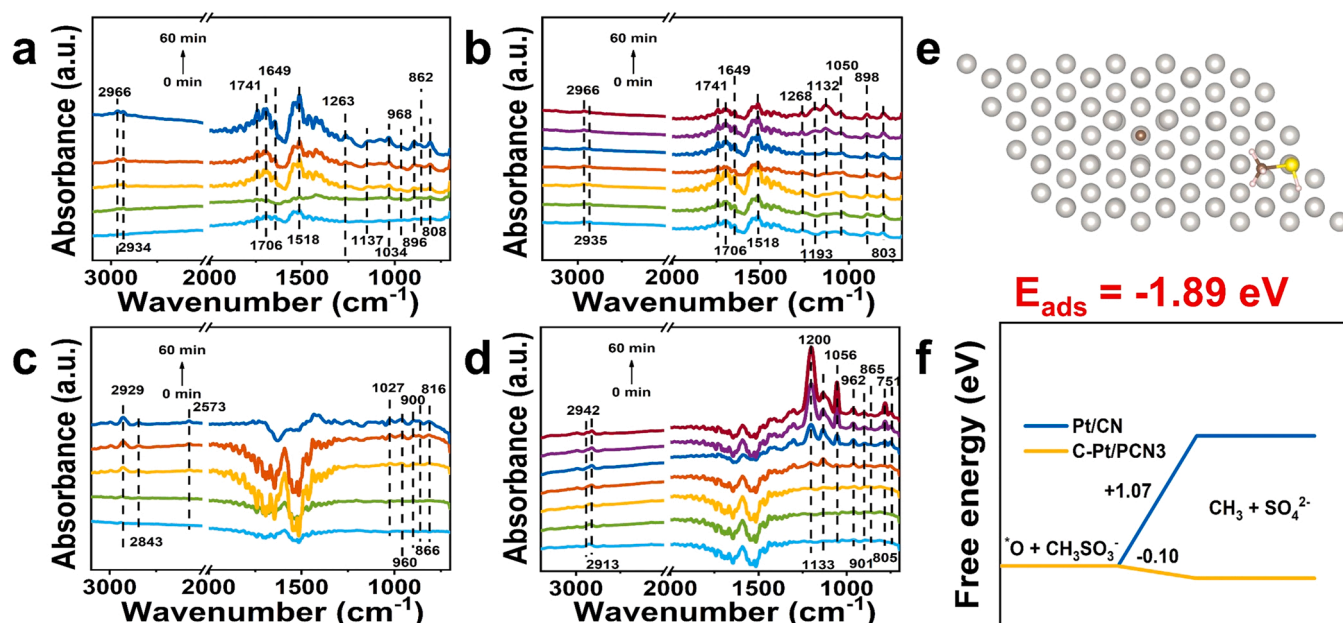


Fig. 5. In-situ DRIFTS in the processes of adsorption (a, c) and catalytic ozonation (b, d) over C-Pt/PCN3 and Pt/CN; (e) The optimized adsorption of CH₃SH molecule on C-Pt/PCN3 coordination structure; (f) Gibbs free energy change of the C—S bond breaking on the surface of C-Pt/PCN3 and Pt/CN. All lengths are given in Å. The silver, yellow, white and brown balls denote Pt, O, H and C atoms, respectively.

proceed spontaneously (+1.07 eV), whereas the C—S bonds were straightforward to break on the surface of C-Pt/PCN3 (−0.10 eV). Combined with the aforementioned analysis, it was concluded that the interstitial C-Pt EMSI structures generated and retained *O with excellent reactivity, as well as lowered the energy barrier of breakage of the C—S bonds, hence promoting the complete mineralization of CH₃SH.

Especially, the resistance of C-Pt/PCN3 to H₂O and SO₄^{2−} was further investigated by DFT calculations. As demonstrated in Fig. S21 and S22, the adsorption energies of H₂O and SO₄^{2−} on C-Pt/PCN3 (−0.28 and −0.81 eV) were greater than those on Pt/CN (−0.66 and −0.91 eV), indicating that the interstitial C-Pt EMSI structures inhibited the adsorption of H₂O and SO₄^{2−} on the surface of C-Pt/PCN3, which was the key factor for C-Pt/PCN3 to maintain excellent stability and water resistance.

4. Conclusion

In this work, the C-Pt/PCN catalysts with the interstitial C-Pt EMSI structures were first developed and identified to boost the synergistic removal of O₃ and CH₃SH. Experimental results showed that the high concentrations of O₃ and CH₃SH were completely removed by the C-Pt/PCN3 catalyst with low Pt loading (0.95 wt%). Notably, the construction of the interstitial C-Pt EMSI structures resulted in a fourfold increase in the intrinsic activity (mass activity) of the Pt catalyst from 56 to 261 ppm mg^{−1}. Moreover, the mass activity of the C-Pt/PCN3 catalyst is 186 times higher than that of commercial MnO₂ (1.4 ppm mg^{−1}) and even surpasses that of the single-atom Pt catalyst (0.5 AD-Pt-G, 111 ppm mg^{−1}).

This study also provided new mechanistic insights into the synergistic control of O₃ and CH₃SH. The interstitial C-based dual-site catalytic structures were proposed and proven to promote the adsorption/activation of O₃ at interstitial C and capture/oxidation of CH₃SH at Pt simultaneously. Moreover, the interstitial C-Pt EMSI structures promoted the electron transfer from Pt to interstitial C, gathering the delocalized electrons of Pt nanoparticles and improving the utilization efficiency of electrons. Therefore, the interstitial C atoms worked as electron shuttles to enable *O formation and subsequently retained *O with excellent reactivity, as well as lowered the energy barrier of C—S

bond breakage, thus achieving efficient decomposition of CH₃SH into CO₂/SO₄^{2−}. The interstitial C-metal EMSI structures could be generalized to other metals that could dissolve C atoms (like Au, Ag, Ni, Pd, etc.), thus efficiently utilizing the delocalized electrons of metal nanoparticles and achieving effective modulation of key intermediates to improve catalytic performance.

CRediT authorship contribution statement

Dingren Ma: Methodology, Investigation, Writing – original draft. **Jing Cao:** Methodology, Visualization. **Kairui Liu:** Methodology, Investigation. **Yexing Zhang:** Methodology. **Qiwen Liang:** Visualization. **Yajing Huang:** Methodology, Software. **Xinyi Guan:** Methodology, Investigation. **Lingling Hu:** Resources. **Chun He:** Supervision. **Dehua Xia:** Methodology, Supervision.

Declaration of Competing Interest

The authors declare that they have no known competing financial interests or personal relationships that could have appeared to influence the work reported in this paper.

Data Availability

Data will be made available on request.

Acknowledgments

This work was supported by the National Natural Science Foundation of China (Nos. 21876212, 21976214, 41603097, 21673086, 52070195), Guangdong Basic and Applied Basic Research Foundation (2022B1515020097, 2019A1515011015, 2021A1515110224), Opening Fund of the State Key Laboratory of Environmental Geochemistry (SKLEG202221), the Science and Technology Program of Guangzhou (201904010353) and Fundamental Research Funds for the Central Universities, Sun Yat-sen University (13lgjc10, 19lgpy157, 22lgqb21) for financially supporting this work.

Appendix A. Supporting information

Supplementary data associated with this article can be found in the online version at [doi:10.1016/j.apcatb.2023.122578](https://doi.org/10.1016/j.apcatb.2023.122578).

References

- [1] Z. Chen, R. Li, D. Chen, Y. Zhuang, B. Gao, L. Yang, M. Li, Understanding the causal influence of major meteorological factors on ground ozone concentrations across China, *J. Clean. Prod.* 242 (2020), 118498.
- [2] T. Wang, L. Xue, P. Brimblecombe, Y.F. Lam, L. Li, L. Zhang, Ozone pollution in China: a review of concentrations, meteorological influences, chemical precursors, and effects, *Sci. Total Environ.* 575 (2017) 1582–1596.
- [3] C. Dong, J.J. Yang, L.H. Xie, G. Cui, W.H. Fang, J.R. Li, Catalytic ozone decomposition and adsorptive VOCs removal in bimetallic metal-organic frameworks, *Nat. Commun.* 13 (2022) 4991.
- [4] Z.B. Sun, Y.N. Si, S.N. Zhao, Q.Y. Wang, S.Q. Zang, Ozone decomposition by a manganese-organic framework over the entire humidity range, *J. Am. Chem. Soc.* 143 (2021) 5150–5157.
- [5] Q. Li, Y. Zhao, C. Ling, S. Yuan, Q. Chen, J. Wang, Towards a comprehensive understanding of the reaction mechanisms between defective MoS_2 and thiol molecules, *Angew. Chem. Int. Ed. Engl.* 56 (2017) 10501–10505.
- [6] C. He, Y. Wang, Z. Li, Y. Huang, Y. Liao, D. Xia, S. Lee, Facet engineered $\alpha\text{-MnO}_2$ for efficient catalytic ozonation of odor CH_3SH : oxygen vacancy-induced active centers and catalytic mechanism, *Environ. Sci. Technol.* 54 (2020) 12771–12783.
- [7] E. Vega, J. Lemus, A. Anfruns, R. Gonzalez-Olmos, J. Palomar, M.J. Martin, Adsorption of volatile sulphur compounds onto modified activated carbons: effect of oxygen functional groups, *J. Hazard. Mater.* 258–259 (2013) 77–83.
- [8] J. Yang, Y. Huang, Y.-W. Chen, D. Xia, C.-Y. Mou, L. Hu, J. Zeng, C. He, P.K. Wong, H.-Y. Zhu, Active site-directed tandem catalysis on $\text{CuO}/\text{V}_2\text{O}_5\text{-MnO}_2$ for efficient and stable catalytic ozonation of S-VOCs under mild condition, *Nano Today* 35 (2020), 100944.
- [9] D. Xia, W. Xu, Y. Wang, J. Yang, Y. Huang, L. Hu, C. He, D. Shu, D.Y.C. Leung, Z. Pang, Enhanced performance and conversion pathway for catalytic ozonation of methyl mercaptan on single-atom Ag deposited three-dimensional ordered mesoporous MnO_2 , *Environ. Sci. Technol.* 52 (2018) 13399–13409.
- [10] S. Zhang, X. Quan, D. Wang, Catalytic ozonation in arrayed zinc oxide nanotubes as highly efficient mini-column catalyst reactors (MCRs): augmentation of hydroxyl radical exposure, *Environ. Sci. Technol.* 52 (2018) 8701–8711.
- [11] G. Yu, Y. Wang, H. Cao, H. Zhao, Y. Xie, Reactive oxygen species and catalytic active sites in heterogeneous catalytic ozonation for water purification, *Environ. Sci. Technol.* 54 (2020) 5931–5946.
- [12] C.T. Campbell, Catalyst-support interactions electronic perturbations, *Nat. Chem.* 4 (2012) 597–598.
- [13] P. Kuang, Y. Wang, B. Zhu, F. Xia, C.-W. Tung, J. Wu, H.M. Chen, J. Yu, Pt single atoms supported on N-doped mesoporous hollow carbon spheres with enhanced electrocatalytic H_2 -evolution activity, *Adv. Mater.* 33 (2021) 2008599.
- [14] K.W. Park, J.H. Choi, B.K. Kwon, S.A. Lee, Y.E. Sung, H.Y. Ha, S.A. Hong, H. Kim, A. Wieckowski, Chemical and electronic effects of Ni in Pt/Ni and Pt/Ru/Ni alloy nanoparticles in methanol electrooxidation, *J. Phys. Chem. B* 106 (2002) 1869–1877.
- [15] L.S. Zhang, X.H. Jiang, Z.A. Zhong, L. Tian, Q. Sun, Y.T. Cui, X. Lu, J.P. Zou, S. L. Luo, Carbon nitride supported high-loading Fe single-atom catalyst for activation of peroxymonosulfate to generate $^1\text{O}_2$ with 100 % selectivity, *Angew. Chem. Int. Ed. Engl.* 60 (2021) 21751–21755.
- [16] Y. Sun, Y. Cao, L. Wang, X. Mu, Q. Zhao, R. Si, X. Zhu, S. Chen, B. Zhang, Chen, Y. Wan, Gold catalysts containing interstitial carbon atoms boost hydrogenation activity, *Nat. Commun.* 11 (2020) 4600.
- [17] S. Vajda, M.J. Pellin, J.P. Greeley, C.L. Marshall, L.A. Curtiss, G.A. Ballentine, J. W. Elam, S. Catillon-Mucherie, P.C. Redfern, F. Mehmood, P. Zapol, Subnanometre platinum clusters as highly active and selective catalysts for the oxidative dehydrogenation of propane, *Nat. Mater.* 8 (2009) 213–216.
- [18] F. Vines, C. Loschen, F. Illas, K.M. Neyman, Edge sites as a gate for subsurface carbon in palladium nanoparticles, *J. Catal.* 266 (2009) 59–63.
- [19] D. Teschner, J. Borsodi, A. Woitsch, Z. Revay, M. Havecker, A. Knop-Gericke, S. D. Jackson, R. Schlögl, The roles of subsurface carbon and hydrogen in palladium-catalyzed alkyne hydrogenation, *Science* 320 (2008) 86–89.
- [20] W. Qu, Z. Tang, W. Liu, Y. Liao, Y. Huang, D. Xia, Q. Lian, S. Tian, C. He, D. Shu, Self-accelerating interfacial catalytic elimination of gaseous sulfur-containing volatile organic compounds as microbubbles in a facet-engineered three-dimensional BiOC sponge fenton-like process, *Environ. Sci. Technol.* 56 (2022) 11657–11669.
- [21] D. Ma, W. Liu, Y. Huang, D. Xia, Q. Lian, C. He, Enhanced catalytic ozonation for eliminating CH_3SH via stable and circular electronic metal-support interactions of $\text{Si}-\text{O}-\text{Mn}$ bonds with low Mn loading, *Environ. Sci. Technol.* 56 (2022) 3678–3688.
- [22] Z. Huang, J.-X. Liang, D. Tang, Y. Chen, W. Qu, X. Hu, J. Chen, Y. Dong, D. Xu, D. Golberg, J. Li, X. Tang, Interplay between remote single-atom active sites triggers speedy catalytic oxidation, *Chem* 8 (2022) 1–10.
- [23] Y. Huang, D. Ma, W. Liu, D. Xia, L. Hu, J. Yang, P. Liao, C. He, Enhanced catalytic ozonation for eliminating CH_3SH via graphene-supported positively charged atomic Pt undergoing $\text{Pt}^{(2+)}/\text{Pt}^{(4+)}$ redox cycle, *Environ. Sci. Technol.* 55 (2021) 16723–16734.
- [24] M. Tian, S. Liu, L. Wang, H. Ding, D. Zhao, Y. Wang, J. Cui, J. Fu, J. Shang, G.K. Li, Complete degradation of gaseous methanol over Pt/FeO_x catalysts by normal temperature catalytic ozonation, *Environ. Sci. Technol.* 54 (2020) 1938–1945.
- [25] E. Rezaei, J. Soltan, N. Chen, J. Lin, Effect of noble metals on activity of $\text{MnO}_x/\gamma\text{-alumina}$ catalyst in catalytic ozonation of toluene, *Chem. Eng. J.* 214 (2013) 219–228.
- [26] W. Li, G.V. Gibbs, S.T. Oyama, Mechanism of ozone decomposition on a manganese oxide catalyst. 1. In situ Raman spectroscopy and ab initio molecular orbital calculations, *J. Am. Chem. Soc.* 120 (1998) 9041–9046.
- [27] J. Bing, C. Hu, L. Zhang, Enhanced mineralization of pharmaceuticals by surface oxidation over mesoporous $\gamma\text{-Ti-Al}_2\text{O}_3$ suspension with ozone, *Appl. Catal. B: Environ.* 202 (2017) 118–126.
- [28] T. Zhang, W. Li, J.P. Croue, Catalytic ozonation of oxalate with a cerium supported palladium oxide: an efficient degradation not relying on hydroxyl radical oxidation, *Environ. Sci. Technol.* 45 (2011) 9339–9346.
- [29] M. Maciejewski, A. Baiker, Incorporation and reactivity of carbon in palladium, *Pure Appl. Chem.* 67 (1995) 1879–1884.
- [30] O. Pique, I.Z. Koleva, F. Vines, H.A. Aleksandrov, G.N. Vayssilov, F. Illas, Subsurface carbon: a general feature of noble metals, *Angew. Chem. Int. Ed. Engl.* 58 (2019) 1744–1748.
- [31] N. Kopfle, T. Gotsch, M. Grunbacher, E.A. Carbonio, M. Havecker, A. Knop-Gericke, L. Schlicker, A. Doran, D. Kober, A. Gurlo, S. Penner, B. Klotzer, Zirconium-assisted activation of palladium to boost syngas production by methane dry reforming, *Angew. Chem. Int. Ed. Engl.* 57 (2018) 14613–14618.
- [32] P. Janthon, F. Viñes, J. Sirijaraensre, J. Limtrakul, F. Illas, Carbon dissolution and segregation in platinum, *Catal. Sci. Technol.* 7 (2017) 807–816.
- [33] Y. Liu, F. Fu, A. McCue, W. Jones, D. Rao, J. Feng, Y. He, D. Li, Adsorbate-induced structural evolution of Pd catalyst for selective hydrogenation of acetylene, *ACS Catal.* 10 (2020) 15048–15059.
- [34] S. Jiang, L. Huang, X. Gao, G. Liu, R. Zhang, Y. Jiao, S. Peng, Q. An, S. Wang, L. Geng, Interstitial carbon induced FCC-Ti exhibiting ultrahigh strength in a $\text{Ti}_{37}\text{Nb}_{28}\text{Mo}_{28}\text{-C}_7$ complex concentrated alloy, *Acta Mater.* 203 (2021), 116456.
- [35] Y. Niu, X. Huang, Y. Wang, M. Xu, J. Chen, S. Xu, M.G. Willinger, W. Zhang, M. Wei, B. Zhang, Manipulating interstitial carbon atoms in the nickel octahedral site for highly efficient hydrogenation of alkyne, *Nat. Commun.* 11 (2020) 3324.
- [36] Y. Gao, T. Wu, C. Yang, C. Ma, Z. Zhao, Z. Wu, S. Cao, W. Geng, Y. Wang, Y. Yao, Y. Zhang, C. Cheng, Activity trends and mechanisms in peroxymonosulfate-assisted catalytic production of singlet oxygen over atomic metal-N-C catalysts, *Angew. Chem. Int. Ed. Engl.* 60 (2021) 22513–22521.
- [37] S. Zhang, L. Chen, Z. Qi, L. Zhuo, J.L. Chen, C.W. Pao, J. Su, G.A. Somorjai, Insights into the mechanism of n-hexane reforming over a single-site platinum catalyst, *J. Am. Chem. Soc.* 142 (2020) 16533–16537.
- [38] Y. Niu, X. Liu, Y. Wang, S. Zhou, Z. Lv, L. Zhang, W. Shi, Y. Li, W. Zhang, D.S. Su, B. Zhang, Visualizing formation of intermetallic PdZn in a palladium/zinc oxide catalyst: interfacial fertilization by PdHx, *Angew. Chem. Int. Ed. Engl.* 58 (2019) 4232–4237.
- [39] Y. Deng, Y. Guo, Z. Jia, J.C. Liu, J. Guo, X. Cai, C. Dong, M. Wang, C. Li, J. Diao, Z. Jiang, J. Xie, N. Wang, H. Xiao, B. Xu, H. Zhang, H. Liu, J. Li, D. Ma, Few-atom Pt ensembles enable efficient catalytic cyclohexane dehydrogenation for hydrogen production, *J. Am. Chem. Soc.* 144 (2022) 3535–3542.
- [40] Y. Wu, P. Zhai, S. Cao, Z. Li, B. Zhang, Y. Zhang, X. Nie, L. Sun, J. Hou, Beyond d orbitals: steering the selectivity of electrochemical CO_2 reduction via hybridized sp band of sulfur-incorporated porous Cd architectures with dual collaborative sites, *Adv. Energy Mater.* 10 (2020) 2002499.
- [41] B.I. Lundqvist, O. Gunnarsson, H. Hjelmberg, J.K. Norskov, Theoretical description of molecule-metal interaction and surface reactions, *Surf. Sci.* 89 (1979) 196–225.
- [42] Q. Xu, G. Li, Y. Zhang, Q. Yang, Y. Sun, C. Felser, Descriptor for hydrogen evolution catalysts based on the bulk band structure effect, *ACS Catal.* 10 (2020) 5042–5048.
- [43] J. Fan, H. Du, Y. Zhao, Q. Wang, Y. Liu, D. Li, J. Feng, Recent progress on rational design of bimetallic Pd based catalysts and their advanced catalysis, *ACS Catal.* 10 (2020) 13560–13583.
- [44] Y. Zhang, J. Liu, J. Wang, Y. Zhao, D. Luo, A. Yu, X. Wang, Z. Chen, Engineering oversaturated Fe-N5 multifunctional catalytic sites for durable lithium-sulfur batteries, *Angew. Chem. Int. Ed. Engl.* 60 (2021) 26622–26629.
- [45] Y. Wang, L. Chen, C. Chen, J. Xi, H. Cao, X. Duan, Y. Xie, W. Song, S. Wang, Occurrence of both hydroxyl radical and surface oxidation pathways in N-doped layered nanocarbons for aqueous catalytic ozonation, *Appl. Catal. B: Environ.* 254 (2019) 283–291.
- [46] Y. Wang, X. Duan, Y. Xie, H. Sun, S. Wang, Nanocarbon-based catalytic ozonation for aqueous oxidation: engineering defects for active sites and tunable reaction pathways, *ACS Catal.* 10 (2020) 13383–13414.
- [47] N. Nishino, K.D. Arquero, M.L. Dawson, B.J. Infrared studies of the reaction of methanesulfonic acid with trimethylamine on surfaces, *Environ. Sci. Technol.* 48 (2014) 323–330.
- [48] S. Zhan, H. Zhang, X. Mi, Y. Zhao, C. Hu, L. Lyu, Efficient fenton-like process for pollutant removal in electron-rich/poor reaction sites induced by surface oxygen vacancy over cobalt-zinc oxides, *Environ. Sci. Technol.* 54 (2020) 8333–8343.